



1 **Simulations of Organic Aerosol Concentrations during Springtime in the Guanzhong**  
2 **Basin, China**

3

4 Tian Feng<sup>1,2,3</sup>, Guohui Li<sup>2,3\*</sup>, Junji Cao<sup>2,3\*</sup>, Naifang Bei<sup>1,2</sup>, Zhenxing Shen<sup>1</sup>, Weijian Zhou<sup>3</sup>, Suixin Liu<sup>2,3</sup>, Ting  
5 Zhang<sup>2,3</sup>, Yichen Wang<sup>2,3</sup>, Xuexi Tie<sup>2,3</sup>, Luisa T. Molina<sup>4</sup>

6

7 <sup>1</sup>School of Human Settlements and Civil Engineering, Xi'an Jiaotong University, Xi'an, Shaanxi, China

8 <sup>2</sup>Key Lab of Aerosol Chemistry and Physics, Institute of Earth Environment, Chinese Academy of Sciences,  
9 Xi'an, Shaanxi, China

10 <sup>3</sup>State Key Laboratory of Loess and Quaternary Geology, Institute of Earth Environment, Chinese Academy of  
11 Sciences, Xi'an, China

12 <sup>4</sup>Molina Center for Energy and the Environment, La Jolla, CA, and Massachusetts Institute of Technology,  
13 Cambridge, MA, USA

14 \*Correspondence to: Guohui Li ([ligh@ieecas.cn](mailto:ligh@ieecas.cn)) and Junji Cao ([jjcao@ieecas.cn](mailto:jjcao@ieecas.cn))

15

16 **Abstract.** The organic aerosol (OA) concentration is simulated in the Guanzhong basin,  
17 China from 23 to 25 April 2013 utilizing the WRF-CHEM model. Two approaches are used  
18 to predict OA concentrations: (1) a traditional secondary organic aerosol (SOA) module; (2) a  
19 non-traditional SOA module including the volatility basis-set modeling method in which  
20 primary organic aerosols (POA) are assumed to be semi-volatile and photochemically  
21 reactive. Generally, the spatial patterns and temporal variations of the calculated hourly  
22 near-surface ozone and fine particle matters agree well with the observations in Xi'an and  
23 surrounding areas. The model also yields reasonable distributions of daily PM<sub>2.5</sub> and  
24 elemental carbon (EC) compared to the filter measurements at 29 sites in the basin. Filter  
25 measured organic carbon (OC) and EC are used to evaluate OA, POA, and SOA using the  
26 OC/EC ratio approach. Compared with the traditional SOA module, the non-traditional  
27 module significantly improves SOA simulations and explains about 88% of the observed  
28 SOA concentration. Oxidation and partitioning of POA treated as semi-volatile constitute the  
29 most important pathway for the SOA formation, contributing more than 75% of the SOA  
30 concentrations in the basin. Residential emissions are the dominant anthropogenic OA source,  
31 constituting about 50% of OA concentrations in urban and rural areas and 30% in the  
32 background area. The OA contribution from transportation emissions decreases from 25% in  
33 urban areas to 20% in the background area, and the industry emission OA contribution is less  
34 than 6%. The simulation results will facilitate the design of the air pollution control strategies  
35 in the basin.

36 **Keywords:** SOA, PM<sub>2.5</sub>, WRF-CHEM Model

37



## 38 1 Introduction

39 Atmospheric aerosols or fine particulate matters ( $PM_{2.5}$ ) influence regional and global  
40 climate directly by absorbing and scattering the solar radiation and indirectly by serving as  
41 cloud condensation nuclei (CCN) and ice nuclei (IN) to modify cloud properties (Seinfeld  
42 and Pandis, 2006). Elevated aerosols also exert adverse impacts on ecosystems and human  
43 health, and reduce the visibility of the atmosphere to cause the haze formation, impairing air  
44 quality (Cao et al., 2012a; 2012b; Greenwald et al., 2006; Seinfeld and Pandis, 2006).

45 OA constitutes one of the most important component of  $PM_{2.5}$  in the atmosphere, with  
46 the mass contribution to  $PM_{2.5}$  ranging from 20% to 90% (Kanakidou et al., 2005; Zhang et  
47 al., 2007). Traditionally, OA is categorized into primary and secondary OA on the basis of its  
48 source and/or formation, referred to as POA and SOA, respectively. POA is emitted into the  
49 atmosphere directly, while SOA forms through complicated chemical reactions of precursors  
50 in the atmosphere. Volatile organic compounds (VOCs) emitted from anthropogenic or  
51 biogenic sources undergo a series of oxidation and gas-particle partitioning to yield SOA,  
52 which has been regarded as a traditional pathway of the SOA formation (Odum et al., 1996;  
53 Pankow, 1994). Recently, semi-volatile POA has been identified to be oxidized continuously  
54 to produce SOA in laboratory studies (Lipsky and Robinson, 2006; Shrivastava et al., 2006).  
55 The mechanism has been parameterized into chemical transport models (Dzepina et al., 2009;  
56 Lane et al., 2008; Li et al., 2011b; Murphy and Pandis, 2009; Robinson et al., 2007;  
57 Shrivastava et al., 2008; Tsimpidi et al., 2010), significantly improving SOA simulations and  
58 capable for closing the gap between the calculated and observed SOA concentrations.

59 China has been suffering severe air pollutions caused by rapid industrialization and  
60 urbanization (Cao et al., 2007; 2005; 2012b; Guinot et al., 2007; He et al., 2015; 2001; Shen  
61 et al., 2009; Tie et al., 2015; Yang et al., 2011; Zhang et al., 2015; 2013). Numerous studies  
62 have shown that OA play an important role in the haze formation in China. Huang et al.



63 (2014) have reported that OA constitute a major fraction (30~50%) of the total  $PM_{2.5}$  in  
64 Beijing, Shanghai, Guangzhou, and Xi'an, and during the severe haze pollution event, SOA  
65 contribute 30~77% of  $PM_{2.5}$  and 44~71% of OA mass concentrations. Using the ACSM  
66 (Aerosol Chemical Speciation Monitor) measurement analyzed by PMF (positive matrix  
67 factorization), Sun et al. (2012) have showed that the oxygenated organic aerosols (OOA, a  
68 surrogate of SOA) dominate OA composition, with a contribution of 64% on average from 26  
69 June to 28 August 2011. Sun et al. (2013) have found that OA account for 52% of the total  
70 non-refractory submicron particulate matters mass loading measured by ACMS during 2012  
71 wintertime in Beijing. Cao et al. (2013) have reported that secondary organic carbon  
72 constitutes 31% of the total carbon utilizing an EC tracer system and isotope mass balance  
73 calculations during the MIRAGE-Shanghai (Megacities Impact on Regional and Global  
74 Environment) campaign in 2009.

75 The Guanzhong basin (GZB) is located in northwestern China and nestled between the  
76 Qinling Mountains on the south and the Loess Plateau on the north (Figure 1), with a  
77 warm-humid climate. The rapid increasing industries and city expansions, as well as the  
78 unique topography, have caused frequent occurrence of haze events in GZB (Shen et al., 2009;  
79 2008). Measurements have shown that carbonaceous aerosols (OA and EC) constitute 48.6%  
80 and 45.9% of  $PM_{2.5}$  mass concentration in fall and winter, respectively in Xi'an, the largest  
81 city of GZB (Cao et al., 2005). Abundant OA has been reported to be directly emitted into the  
82 atmosphere from anthropogenic emissions, such as residential and transportation sources in  
83 GZB (Cao et al., 2005). High SOA level has been observed in GZB during wintertime  
84 (Huang et al., 2014). However, the source and formation of OA and especially SOA in GZB  
85 still remain obscure. During the period from 20 to 26 April 2013, a field campaign was  
86 conducted to identify the OA distribution and sources in GZB and an episode during 23-25  
87 April was simulated to identify the OA sources in this study. Daily filter measurements at 29



88 sites in GZB were collected, and EC and OC were analyzed in  $PM_{2.5}$ , which provides a good  
89 opportunity for better understanding OA and particularly SOA sources and formation in GZB.

90 The purpose of the present study is to investigate the formation and source  
91 apportionments of OA and SOA in GZB during springtime using the WRF-CHEM model.  
92 The WRF-CHEM model and its configuration are described in Section 2. The model results  
93 and discussions are presented in Section 3, and the conclusions are summarized in Section 4.

94

## 95 **2 Model and Method**

### 96 **2.1 WRF-CHEM Model**

97 A specific version of the WRF-CHEM model (Grell et al., 2005) developed by Li et al.  
98 (2011b; 2011a; 2012; 2010) at Molina Center for Energy and the Environment (MCE2) is  
99 utilized to investigate the OA formation in GZB. This version employs a flexible gas-phase  
100 chemical module and the CMAQ (version 4.6) aerosol module developed by US EPA  
101 (Binkowski and Roselle, 2003). The dry deposition of chemical species is parameterized  
102 according to Wesely (1989) and the wet deposition follows the method in CMAQ. The FTUV  
103 module (Li et al., 2005; Tie et al., 2003) considering the impacts of aerosols and clouds on  
104 photochemistry is used to calculate the photolysis rates. The ISORROPIA Version 1.7  
105 (<http://nenes.eas.gatech.edu/ISORROPIA/>) is employed to the WRF-CHEM model to  
106 simulate the inorganic aerosols.

### 107 **2.2 Secondary Organic Aerosol Modules**

108 Two kinds of SOA modules are utilized in the WRF-CHEM model simulations: a  
109 traditional 2-product SOA module (T2-SOA module) and a non-traditional SOA module  
110 (NT-SOA module) (Li et al., 2011b).

111 In the T2-SOA module, SOA concentrations are predicted from the oxidation of six  
112 lumped organic species, including alkanes, alkenes, cresol, high-yield aromatics, low-yield



113 aromatics, and monoterpenes, following the method developed by Schell et al. (2001).

114 The NT-SOA module simulates SOA formation based on the volatility basis-set (VBS)  
115 method (Donahue et al., 2006; Robinson et al., 2007). In the module, the POA is distributed  
116 in logarithmically spaced volatility bins and assumed to be semi-volatile and photochemically  
117 reactive (Li et al., 2011b). Nine surrogate species with saturation concentration ranging from  
118  $10^{-2}$  to  $10^6$   $\mu\text{g m}^{-3}$  at room temperature are selected to represent POA components following  
119 (Shrivastava et al., 2008). The SOA formation from glyoxal and methyglyoxal is  
120 parameterized as a first-order irreversible uptake by aerosol particles with a reactive uptake  
121 coefficient of  $3.7 \times 10^{-3}$  (Volkamer et al., 2007; Zhao et al., 2006). Detailed information about  
122 T2-SOA and NT-SOA modules can be found in Li et al. (2011b).

### 123 **2.3 Model Configuration**

124 In this study, a three-day episode from 23 to 25 April 2013 is simulated in association  
125 with the filter measurements of  $\text{PM}_{2.5}$ , OC, and EC in GZB. The model is configured with a  
126 horizontal grid spacing of 3 km and  $200 \times 200$  grids which is centered at  $34.25^\circ\text{N}$  and  $109^\circ\text{E}$   
127 (Figure 1). In the vertical direction, we use thirty-five levels in a stretched vertical grid with  
128 spacing ranging from 50 m near the surface to 500 m at 2.5 km above ground level and 1 km  
129 above 14 km. The physics and dynamics of the configuration adopt the microphysics scheme  
130 of Hong and Lim (2006), the Yonsei University planetary boundary layer scheme (Hong et al.,  
131 2006), the land surface scheme of 5-layer thermal diffusion (Dudhia, 1996), the Dudhia  
132 shortwave scheme (Dudhia, 1989) and the rapid radiative transfer model (RRTM) longwave  
133 scheme (Mlawer et al., 1997). No cumulus parameterization is used due to the high horizontal  
134 resolution. The NCEP  $1^\circ \times 1^\circ$  reanalysis data are used for the meteorological initial and  
135 boundary conditions. The chemical initial and boundary conditions are interpolated from  
136 Model for OZone And Related chemical Tracers (MOZART) output with a 6-hour interval  
137 (Horowitz et al., 2003). The spin-up time for the simulation is one day.



138 The anthropogenic emission inventory (EI) including agriculture, industry, power plant,  
139 residential, and transportation sources is developed by Zhang et al. (2009). Figure 2 shows  
140 the monthly POA and VOCs emissions in GZB along with the Xi'an urban area. Large  
141 anthropogenic emissions are concentrated in Xi'an and surrounding areas. The POA from the  
142 transportation source and biomass burning are redistributed following Tsimpidi et al. (2010).  
143 The MEGAN model is used to on-line calculate the biogenic emissions in the model  
144 (Guenther et al., 2006).

#### 145 2.4 Statistical Methods for Comparisons

146 The mean bias (*MB*), root mean square error (*RMSE*), and index of agreement (*IOA*)  
147 are used to evaluate the model performance in simulating gas-phase species and aerosols.

$$148 \quad MB = \frac{1}{N} \sum_{i=1}^N (P_i - O_i) \quad (1)$$

$$149 \quad RMSE = \left[ \frac{1}{N} \sum_{i=1}^N (P_i - O_i)^2 \right]^{\frac{1}{2}} \quad (2)$$

$$150 \quad IOA = 1 - \frac{\sum_{i=1}^N (P_i - O_i)^2}{\sum_{i=1}^N (|P_i - \bar{O}| + |O_i - \bar{O}|)^2} \quad (3)$$

151 where  $P_i$  and  $O_i$  are the predicted and observed variables, respectively.  $N$  is the total  
152 number of the predictions for comparison and  $\bar{O}$  donate the average of the observation. The  
153 *IOA* ranges from 0 to 1, with 1 showing a perfect agreement of the prediction with the  
154 observation.

155

### 156 3 Results and Discussions

#### 157 3.1 Model Performance

158 The meteorological fields are of essential importance for the simulation of chemical  
159 species concentrations in time evolution and spatial distribution (Bei et al., 2008; 2010; 2012).



160 In the present study, the observations of temperature, pressure, relative humidity, and wind  
161 components at 50 meteorological stations in GZB are assimilated in the WRF-CHEM model  
162 simulations using the four-dimension data assimilation (FDDA) to improve the simulation of  
163 meteorological fields. Model performance is validated using the hourly ozone ( $O_3$ ) and  $PM_{2.5}$   
164 observations at 13 monitoring sites in Xi'an and surrounding areas, released by the Ministry  
165 of Environmental Protection of China (China MEP), and daily filter measurement of  $PM_{2.5}$ ,  
166 EC, and OC at 29 sites in GZB.

### 167 3.1.1 Hourly $O_3$ and $PM_{2.5}$ Simulations in Xi'an and Surrounding Areas

168 Figures 3 and 4 provide the spatial patterns of observed and simulated near-surface  $O_3$   
169 and  $PM_{2.5}$  mass concentrations at 08:00 and 15:00 Beijing Time (BJT) from April 23 to 25,  
170 2013 in Xi'an and surrounding areas, along with simulated wind fields. The calculated  $O_3$  and  
171  $PM_{2.5}$  spatial distributions are generally consistent with the observations at the monitoring  
172 sites. At 08:00 BJT, the near-surface winds are weak or calm, and the low planetary boundary  
173 layer (PBL) also facilitates the accumulation of pollutants, causing observed and simulated  
174 high near-surface  $PM_{2.5}$  mass concentrations. The  $PM_{2.5}$  mass concentration frequently  
175 exceeds  $150 \mu g m^{-3}$ , causing heavy air pollutions in Xi'an and surrounding areas. Weak solar  
176 insolation slows the photochemical activities and the low PBL is also favorable for buildup of  
177 emitted  $NO_x$ , significantly lowering the  $O_3$  level at 08:00 BJT, and the calculated and  
178 observed near-surface  $O_3$  concentrations range from 20 to  $30 \mu g m^{-3}$ . At 15:00 BJT, with the  
179 development of PBL and enhancement of winds, the  $PM_{2.5}$  mass concentrations are decreased  
180 but still remain high level in Xi'an and surrounding areas on April 23 and 24. The strong  
181 divergence at 15:00 BJT on April 25 efficiently disperses the  $PM_{2.5}$  accumulated in the  
182 morning and remarkably improves the air quality in Xi'an and surrounding areas. The  $O_3$   
183 mass concentration are substantially increased to more than  $80 \mu g m^{-3}$  at 15:00 BJT with the  
184 enhancement of photochemical activities.



185 Figure 5 presents the temporal variations of calculated and measured  $O_3$  and  $PM_{2.5}$   
186 concentrations averaged over 13 monitoring sites in Xi'an and surrounding areas from April  
187 23 to 25, 2013. The WRF-CHEM model generally replicates the observed  $O_3$  variations  
188 during the episode, i.e., the occurrence of peak  $O_3$  concentrations in the afternoon due to  
189 active photochemical processes and rapid falloff during nighttime caused by the  $NO_x$  titration.  
190 The *MB* and *RMSE* are  $7.1 \mu\text{g m}^{-3}$  and  $21.3 \mu\text{g m}^{-3}$ , respectively, and the *IOA* is 0.89. The  
191 model considerably overestimates the observed  $O_3$  concentration on April 23, perhaps due to  
192 the high  $O_3$  background transport. However, on April 25, the model notably underestimates  
193 the peak  $O_3$  concentration in the afternoon, which is caused by the simulated strong  
194 divergence in Xi'an and surrounding areas (Figure 3). In Figure 5, the observed  $PM_{2.5}$   
195 variations are reasonably well reproduced by the model, although overestimations and  
196 underestimations still exist. The *MB* and *RMSE* are  $8.1 \mu\text{g m}^{-3}$  and  $23.9 \mu\text{g m}^{-3}$ , respectively,  
197 and the *IOA* is 0.86. The observed and simulated  $PM_{2.5}$  mass concentrations both show that  
198 during the three-day episode, the air quality in Xi'an and surrounding areas gradually  
199 improves, with the  $PM_{2.5}$  concentration decreased from about  $160 \mu\text{g m}^{-3}$  in the morning on  
200 April 23 to about  $50 \mu\text{g m}^{-3}$  in the afternoon on April 25. The  $PM_{2.5}$  mass concentrations are  
201 generally elevated in the morning during the episode, caused by weak or calm horizontal  
202 winds and slow development of PBL.

### 203 3.1.2 Daily $PM_{2.5}$ and EC Simulations in GZB

204 Daily filter measurements of  $PM_{2.5}$  and EC mass concentrations at 29 sites in GZB  
205 (squares in Figure 1) are used to further verify the WRF-CHEM model simulations. Figure 6  
206 shows the scatter plots of calculated and measured daily  $PM_{2.5}$  and EC mass concentrations at  
207 29 sites during the episode. The simulated daily  $PM_{2.5}$  mass concentrations are generally in  
208 agreement with the filter measurement over 29 sites. The  $PM_{2.5}$  concentration averaged over  
209 29 sites during the episode is  $79 \mu\text{g m}^{-3}$ , close to the observed  $87 \mu\text{g m}^{-3}$ . The *MB* and *RMSE*



210 of  $PM_{2.5}$  mass concentrations are  $-7.4 \mu\text{g m}^{-3}$  and  $10.3 \mu\text{g m}^{-3}$ , showing a reasonable  $PM_{2.5}$   
211 simulation in GZB. The WRF-CHEM model slightly overestimates the observed EC mass  
212 concentrations, with the *MB* of  $0.2 \mu\text{g m}^{-3}$  and the *RMSE* of  $0.6 \mu\text{g m}^{-3}$ .

213 The calculated daily spatial patterns of  $PM_{2.5}$  and EC mass concentrations are displayed  
214 in Figure 7 along with the measurements at the 29 sites. The simulated distributions of  $PM_{2.5}$   
215 and EC mass concentrations are consistent well with the filter measurements. On April 23,  
216 the eastern part of GZB is the most polluted area, with the daily  $PM_{2.5}$  mass concentrations  
217 exceeding  $115 \mu\text{g m}^{-3}$ . The daily  $PM_{2.5}$  mass concentrations are still high on April 24,  
218 exceeding  $75 \mu\text{g m}^{-3}$  over most of the area in GZB. The air quality in GZB is considerably  
219 improved on April 25, and the daily  $PM_{2.5}$  mass concentrations are generally less than  $75 \mu\text{g}$   
220  $\text{m}^{-3}$  in the north part of GZB. The EC distributions do not exhibit remarkable variations from  
221 April 23 to 25, indicating that the EC levels are primarily determined by direct emissions. In  
222 addition, although the daily  $PM_{2.5}$  mass concentrations decrease substantially from April 23  
223 to 25, the variations of EC mass concentrations are not so significant.

224 The simulated distributions of the column-integrated aerosol optical depth (AOD) at  
225 550 nm are verified using the available measurements from the MODIS (Moderate  
226 Resolution Imaging Spectroradiometer) aerosol level-2 product in Figure 8. The retrieved  
227 AOD shows that GZB suffers severe air pollutions at 12:00 BJT on 24 April, and the most  
228 contaminated area is Xi'an and surrounding areas with AOD more than 1.2. The model  
229 successfully reproduces the retrieved AOD spatial pattern in GZB, but underestimates the  
230 retrieved AOD in the north of GZB, which might be caused by the underestimation of dust  
231 aerosols. At 11:00 BJT on 25 April, the model underestimates the retrieved AOD in the west  
232 part of GZB, perhaps due to the biases of simulated relative humidity.

233 The WRF-CHEM model generally well reproduces  $O_3$  and  $PM_{2.5}$  concentrations in  
234 Xi'an and surrounding areas, and the daily EC and  $PM_{2.5}$  mass concentrations in GZB,



235 indicating that meteorological fields are well simulated and the emissions used are also  
236 reasonable in the study.

### 237 **3.2 Organic Aerosols in GZB**

238 The OC/EC ratio approach is employed to evaluate the OA concentration from the filter  
239 measured OC and EC concentrations (Strader, 1999). Previous studies using the OC/EC ratio  
240 approach have been extensively conducted in China (Cao et al., 2003; 2004). Cao et al. (2007)  
241 have analyzed the OC and EC concentrations in 14 cities over China in 2003 and proposed  
242 primary OC/EC ratios of 2.81 for northern cities in winter, 2.10 for southern cities in winter,  
243 1.99 for northern cities in summer, and 1.29 for southern cities in summer. To estimate the  
244 primary OC (POC) and secondary OC (SOC) concentrations during April 2013 in GZB, a  
245 POC/EC ratio of 2.4 is used to derive POC and SOC from OC and EC measurements.  
246 Numerous studies have been performed to investigate the POA/POC and SOA/SOC ratios  
247 (Aiken et al., 2008; Yu, 2011; Yu et al., 2009), which can be used to obtain OA  
248 concentrations from measured OC concentrations. In the present study, a POA/POC ratio of  
249 1.2 and a SOA/SOC ratio of 1.6 are adopted to obtain POA and SOA concentrations, as well  
250 as OA concentrations.

#### 251 **3.2.1 OA Simulations from the T2-SOA and NT-SOA modules**

252 Figure 9a shows that the scatterplot of the observed and simulated OA concentrations at  
253 29 sites during the episode. Apparently, both the T2-SOA and NT-SOA modules reasonably  
254 replicate the observed OA mass concentrations in GZB, and the OA difference between the  
255 two modules is not remarkable, as shown in Figure 9a. The T2-SOA module overestimates  
256 the observed OA concentrations by about 33.6% averaged over the 29 sites, and the NT-SOA  
257 modules underestimates the observation by about 4.3%. Although the T2-SOA and NT-SOA  
258 modules both reproduce comparable OA levels against the measurements, the simulated OA  
259 components, i.e. POA and SOA, differ greatly between the two modules. Figures 9b and 9c



260 provide comparisons of the simulated POA and SOA concentrations from the T2-SOA and  
261 NT-SOA modules with the measurements, respectively. The T2-SOA module overestimates  
262 the measured POA by around 132.0%, and only explains about 9.4% of the observed SOA  
263 concentration. The SOA simulations are comparable to Li et al. (2011b), in which the  
264 T2-SOA module fails to yield sufficient SOA concentrations to match the observations by a  
265 factor of 7. As a comparison, the NT-SOA module overestimates the observed POA by 17.5%  
266 and explains around 87.7% of the observed SOA concentration, significantly improving the  
267 POA and SOA simulations.

268 Figure 10 presents the temporal variations of simulated SOA mass concentrations in  
269 Xi'an and surrounding areas from the T2-SOA and NT-SOA modules, respectively. The  
270 diurnal variations from the two models agree well with each other, with peak occurrence at  
271 noontime, caused by the enhanced photochemical activities. The NT-SOA module  
272 remarkably improves the SOA yields during the entire episode to around  $10 \mu\text{g m}^{-3}$ , about  
273 tenfold increase compared with the simulations from the T2-SOA module.

### 274 3.2.2 Urban, Rural and Background POA and SOA

275 Since the NT-SOA module significantly improves the model performance in simulating  
276 POA and SOA in GZB, Figure 11 displays the spatial distributions of OA, POA, and SOA  
277 simulated by the NT-SOA module against the measurement in GZB. The simulated OA, POA,  
278 and SOA patterns are generally in agreement with the observations, but the model frequently  
279 underestimates the observations in the north part of GZB (Figure 11). Both the simulation  
280 and the measurement show that the entire GZB is OA contaminated during the simulation  
281 episode ( $20 \mu\text{g m}^{-3}$  and above) (Figures 11a-c). POA is primarily concentrated in the central  
282 part of GZB, directly linked to the source region (Figures 11d-f). However, SOA is dispersed  
283 efficiently in the horizontal direction, showing the rapid aging process of OA. The  
284 simulations reveal a progressive increase of SOA concentrations in background areas, which



285 is consistent with the measurements at the background site (red squares in Figures 11g-i).

286 The comparisons of the calculated and measured SOA mass fractions in OA at urban,  
287 rural and background sites are displayed in Figure 12. The 29 sites are categorized into three  
288 types based on their locations: 18 urban sites, 10 rural sites, and 1 background site, as shown  
289 in Figure 1b. The average mass fractions over each type of the sites are colored red. The mass  
290 fractions of SOA in OA at urban and rural sites are very close (around 44%~50% from the  
291 observations and around 40% from the simulation on average), suggesting a similar OA aging  
292 process in urban and rural areas of GZB. The SOA mass fraction at the background site is  
293 much higher, which well agrees with the observations (around 85% from the observations  
294 and around 70% from the simulation on average), indicating that the OA in background areas  
295 undergoes long-time aging processes.

296 The SOA formation pathways considered in the NT-SOA module include (1) oxidation  
297 of anthropogenic VOCs (ASOA), (2) oxidation of biogenic VOCs (BSOA), (3) oxidation and  
298 partitioning of POA treated as semi-volatile (PSOA), and (4) irreversible uptake of glyoxal  
299 and methylglyoxal on aerosol surfaces (GSOA). The SOA mass fractions in OA increase  
300 from 35.1% at urban sites to 40.4% at rural sites, and sharply to 71.0% at the background site  
301 (Table 1). PSOA dominate SOA mass concentrations at all sites, and its contribution to SOA  
302 increases from 79.4% at urban sites to 88.8% at the background site, showing the continuous  
303 aging process of OA (Figure 13). The SOA contribution from ASOA and GSOA decreases  
304 from urban sites to the background site, showing the abatement of direct anthropogenic  
305 impacts. At urban sites, ASOA, BSOA, and GSOA contribute comparably to the SOA mass  
306 concentration. At the background site, the SOA contribution from ASOA and GSOA is very  
307 low, less than 3%. The GSOA constitutes about 10% of SOA mass in the afternoon at urban  
308 sites, close to the results of Li et al. (2011b) in Mexico City.



### 309 **3.2.4 Contributions of Anthropogenic Emissions to OA**

310 Sensitivity studies are conducted to verify the contributions from anthropogenic  
311 emissions including industry, residential and transportation sources to the OA mass  
312 concentrations during the episode. The factor separation approach (FSA) proposed by Stein  
313 and Alpert (1993) is utilized to decompose the contribution from an individual source. The  
314 simulation with all anthropogenic emissions is taken as the base case (referred to as BAS case)  
315 to compare with the sensitivity studies. Four sensitivity studies are performed, including (1)  
316 ANT case without all anthropogenic emissions, (2) RES case without the residential emission,  
317 (3) IND case without the industry emission, and (4) TRA case without the transportation  
318 emission in simulations. According to the FSA approach, the OA contribution from an  
319 individual source, i.e., residential emissions, can be calculated as  $OA(BAS) - OA(RES)$ .

320 Anthropogenic emissions dominate the OA level at the urban and rural sites, with the  
321 OA contribution of 82.4% ( $18.2 \mu\text{g m}^{-3}$ ) and 77.3% ( $12.8 \mu\text{g m}^{-3}$ ), respectively (Table 2). At  
322 the background site, the OA contribution from anthropogenic emissions is close to 60% ( $4.7$   
323  $\mu\text{g m}^{-3}$ ), showing that the background area is still substantially influenced by human activities  
324 despite the far distance from the urban area. The residential emission is the most important  
325 anthropogenic OA source at the urban and rural sites, with the OA contribution close to 50%,  
326 indicating that reducing residential emission is an efficient approach for OA mitigation in  
327 GZB. The OA contribution from the transportation source is 25.0% at the urban sites,  
328 exceeding 20.3% at the rural sites and 19.8% at the background sites. The industry emission  
329 is not an important OA source in GZB, with the contribution less than 6.1%. It is worth to  
330 note that, the OA contributions from residential, transportation, and industry emissions are  
331 comparable at the urban and rural sites, indicating that the OA source difference between the  
332 rural and urban area has been rapidly diminishing due to urbanization and industrialization in  
333 GZB.



334

#### 335 **4 Summary and Conclusions**

336 A 3-day episode from 23 to 25 April 2013 is simulated in the Guanzhong basin, China  
337 using the WRF-CHEM model to investigate the SOA formation and verify the OA source. We  
338 use two SOA approaches to simulate OA: a traditional 2-product SOA module and a  
339 non-traditional SOA module including VBS modeling method and the SOA contribution from  
340 dicarbonyl compounds. Meteorological observations during the simulation period are  
341 assimilated using the FDDA method in WRF-CHEM simulations. Model results are  
342 compared with hourly O<sub>3</sub> and PM<sub>2.5</sub> measurements in Xi'an and GZB.

343 The WRF-CHEM model generally well simulates the spatial distributions and temporal  
344 variations of near-surface O<sub>3</sub> and PM<sub>2.5</sub>, but biases still exist due to the uncertainties of  
345 meteorological fields and emission inventories. The model performs reasonably well in  
346 reproducing the distribution of the filter measured daily PM<sub>2.5</sub> and EC in GZB, but  
347 underestimates the observed PM<sub>2.5</sub> mass concentration by 7.4 μg m<sup>-3</sup> on average.

348 The OC/EC ratio approach is used to evaluate OA, POA, and SOA concentrations from  
349 the filter measured OC and EC concentrations. The traditional and non-traditional SOA  
350 modules both yields reasonable OA simulations compared with measurements, but perform  
351 differently in simulating POA and SOA. The traditional module overestimates the measured  
352 POA concentration by around 132.0% but underestimates the observed SOA concentration by  
353 a factor of 10. The non-traditional module overestimates the observed POA concentration by  
354 17.5% and explains around 87.7% of the observed SOA concentration, significantly  
355 improving the POA and SOA simulations. Although the model can produce similar PM<sub>2.5</sub>  
356 simulations when using the traditional and non-traditional SOA modules, the results might  
357 cause misleading when the traditional SOA module is used to devise the PM<sub>2.5</sub> mitigation  
358 strategy.



359 Simulations from the non-traditional SOA module show that oxidation and partitioning  
360 of POA which is treated as semi-volatile in the model dominate the SOA concentration in  
361 GZB, with the SOA contribution exceeding 75% and also gradually increasing from urban  
362 sites to the background site. The oxidation of anthropogenic and biogenic VOCs and the  
363 irreversible uptake of dicarbonyl compounds do not constitute an important SOA formation  
364 pathway in GZB, with the SOA contributions less than 10% generally. Anthropogenic  
365 emissions are the dominant OA source at urban and rural sites, contributing over 70% of OA  
366 concentrations. Residential emissions are the most important anthropogenic OA sources,  
367 constituting about 50% of OA concentrations at urban and rural sites and 30.2% at the  
368 background site. Transportation emissions make up 25.0% of the OA concentrations at urban  
369 sites and decreasing to 19.8% at the background site. The OA contribution from industry  
370 emissions is not significant, less than 6.1% in GZB.

371 Although the WRF-CHEM model reasonably well predicts the patterns and variations  
372 of observed  $O_3$ ,  $PM_{2.5}$ , and aerosol components, biases still exist. Considering uncertainties  
373 from measurements, emissions, meteorological fields, and the SOA modules, future studies  
374 need to be performed to further improve SOA simulations and OA source apportionment, to  
375 provide the underlying basis for better understanding the haze formation and support the  
376 design and implementation of emission control strategies in the Guanzhong basin.

377

378 **Data availability:** The real-time  $O_3$  and  $PM_{2.5}$  are accessible for the public on the website  
379 <http://106.37.208.233:20035/>. One can also access the historic profile of observed ambient  
380 pollutants through visiting <http://www.aqistudy.cn/>.

381

382



383 *Acknowledgements.* This work was supported by the National Natural Science Foundation of  
384 China (No. 41275153) and supported by the "Strategic Priority Research Program" of the  
385 Chinese Academy of Sciences, Grant No. XDB05060500. Guohui Li is also supported by the  
386 "Hundred Talents Program" of the Chinese Academy of Sciences. Naifang Bei is supported  
387 by the National Natural Science Foundation of China (No. 41275101).

388

389

390

391

392 **References**

- 393 Aiken, A. C., DeCarlo, P. F., Kroll, J. H., Worsnop, D. R., Huffman, J. A., Docherty, K. S.,  
394 Ulbrich, I. M., Mohr, C., Kimmel, J. R., Sueper, D., Sun, Y., Zhang, Q., Trimborn, A.,  
395 Northway, M., Ziemann, P. J., Canagaratna, M. R., Onasch, T. B., Alfarra, M. R., Prévôt,  
396 A. S. H., Dommen, J., Duplissy, J., Metzger, A., Baltensperger, U. and Jimenez, J. L.:  
397 O/C and OM/OC Ratios of Primary, Secondary, and Ambient Organic Aerosols with  
398 High-Resolution Time-of-Flight Aerosol Mass Spectrometry, *Environ. Sci. Technol.*,  
399 42(12), 4478–4485, doi:10.1021/es703009q, 2008.
- 400 Bei, N., de Foy, B., Lei, W., Zavala, M. and Molina, L. T.: Using 3DVAR data assimilation  
401 system to improve ozone simulations in the Mexico City basin, *Atmos. Chem. Phys.*,  
402 8(24), 7353–7366, doi:10.5194/acp-8-7353-2008, 2008.
- 403 Bei, N., Lei, W., Zavala, M. and Molina, L. T.: Ozone predictabilities due to meteorological  
404 uncertainties in the Mexico City basin using ensemble forecasts, *Atmos. Chem. Phys.*,  
405 10(13), 6295–6309, doi:10.5194/acp-10-6295-2010, 2010.
- 406 Bei, N., Li, G. and Molina, L. T.: Uncertainties in SOA simulations due to meteorological  
407 uncertainties in Mexico City during MILAGRO-2006 field campaign, *Atmos. Chem.*  
408 *Phys.*, 12(23), 11295–11308, doi:10.5194/acp-12-11295-2012, 2012.
- 409 Binkowski, F. S. and Roselle, S. J.: Models-3 Community Multiscale Air Quality (CMAQ)  
410 model aerosol component 1. Model description, *J. Geophys. Res.*, 108(D6), 4183–18,  
411 doi:10.1029/2001JD001409, 2003.
- 412 Cao, J. J., Lee, S. C., Chow, J. C., Watson, J. G., Ho, K. F., Zhang, R. J., Jin, Z. D., Shen, Z.  
413 X., Chen, G. C., Kang, Y. M., Zou, S. C., Zhang, L. Z., Qi, S. H., Dai, M. H., Cheng, Y.  
414 and Hu, K.: Spatial and seasonal distributions of carbonaceous aerosols over China, *J.*  
415 *Geophys. Res.*, 112(D22), D22S11–9, doi:10.1029/2006JD008205, 2007.
- 416 Cao, J. J., Lee, S. C., Ho, K. F., Zhang, X. Y. and Zou, S. C.: Characteristics of carbonaceous  
417 aerosol in Pearl River Delta Region, China during 2001 winter period, *Atmos. Environ.*,  
418 37(11), 1451–1460, doi:10.1016/s1352-2310(02)01002-6, 2003.
- 419 Cao, J. J., Lee, S. C., Ho, K. F., Zou, S. C., Fung, K., Li, Y., Watson, J. G. and Chow, J. C.:  
420 Spatial and seasonal variations of atmospheric organic carbon and elemental carbon in  
421 Pearl River Delta Region, China, *Atmos. Environ.*, 38(27), 4447–4456,  
422 doi:10.1016/j.atmosenv.2004.05.016, 2004.
- 423 Cao, J. J., Wu, F., Chow, J. C., Lee, S. C. and Li, Y.: Characterization and source  
424 apportionment of atmospheric organic and elemental carbon during fall and winter of  
425 2003 in Xi'an, China, *Atmos. Chem. Phys.*, 5(11), 3127–3137,  
426 doi:10.5194/acp-5-3127-2005, 2005.
- 427 Cao, J. J., Zhu, C. S., Tie, X. X., Geng, F. H., Xu, H. M., Ho, S. S. H., Wang, G. H., Han, Y.  
428 M. and Ho, K. F.: Characteristics and sources of carbonaceous aerosols from Shanghai,  
429 China, *Atmos. Chem. Phys.*, 13(2), 803–817, doi:10.5194/acp-13-803-2013, 2013.
- 430 Cao, J., Xu, H., Xu, Q., Chen, B. and Kan, H.: Fine particulate matter constituents and  
431 cardiopulmonary mortality in a heavily polluted Chinese city, *Environ. Health Perspect.*,  
432 120(3), 373–378, doi:10.1289/ehp.1103671, 2012a.
- 433 Cao, J.-J., Wang, Q.-Y., Chow, J. C., Watson, J. G., Tie, X.-X., Shen, Z.-X., Wang, P. and  
434 An, Z.-S.: Impacts of aerosol compositions on visibility impairment in Xi'an, China,  
435 *Atmos. Environ.*, 59, 559–566, doi:10.1016/j.atmosenv.2012.05.036, 2012b.



- 436 Donahue, N. M., Robinson, A. L., Stanier, C. O. and Pandis, S. N.: Coupled Partitioning,  
437 Dilution, and Chemical Aging of Semivolatile Organics, *Environ. Sci. Technol.*, 40(8),  
438 2635–2643, doi:10.1021/es052297c, 2006.
- 439 Dudhia, J.: Numerical study of convection observed during the winter monsoon experiment  
440 using a mesoscale two-dimensional model, *J. Atmos. Sci.*, 46(20), 3077–3107,  
441 doi:10.1175/1520-0469(1989)046<3077:NSOCOD>2.0.CO;2, 1989.
- 442 Dudhia, J.: A multi-layer soil temperature model for MM5, Preprints, 49–50, 1996.
- 443 Dzepina, K., Volkamer, R. M., Madronich, S., Tulet, P., Ulbrich, I. M., Zhang, Q., Cappa, C.  
444 D., Ziemann, P. J. and Jimenez, J. L.: Evaluation of recently-proposed secondary organic  
445 aerosol models for a case study in Mexico City, *Atmos. Chem. Phys.*, 9(15), 5681–5709,  
446 doi:10.5194/acp-9-5681-2009, 2009.
- 447 Greenwald, R., Bergin, M. H., Xu, J. and Cohan, D.: The influence of aerosols on crop  
448 production: A study using the CERES crop model, *Agr. Syst.*, 89(2-3), 390–413,  
449 doi:10.1016/j.agsy.2005.10.004, 2006.
- 450 Grell, G. A., Peckham, S. E., Schmitz, R., McKeen, S. A., Frost, G., Skamarock, W. C. and  
451 Eder, B.: Fully coupled “online” chemistry within the WRF model, *Atmos. Environ.*,  
452 39(37), 6957–6975, doi:10.1016/j.atmosenv.2005.04.027, 2005.
- 453 Guenther, A., Karl, T., Harley, P., Wiedinmyer, C., Palmer, P. I. and Geron, C.: Estimates of  
454 global terrestrial isoprene emissions using MEGAN (Model of Emissions of Gases and  
455 Aerosols from Nature), *Atmos. Chem. Phys.*, 6(11), 3181–3210,  
456 doi:10.5194/acp-6-3181-2006, 2006.
- 457 Guinot, B., Cachier, H., Sciare, J., Tong, Y., Xin, W. and Jianhua, Y.: Beijing aerosol:  
458 Atmospheric interactions and new trends, *J. Geophys. Res.*, 112(D14), D14314–16,  
459 doi:10.1029/2006JD008195, 2007.
- 460 He, H., Tie, X., Zhang, Q., Liu, X., Gao, Q., Li, X. and Gao, Y.: Analysis of the causes of  
461 heavy aerosol pollution in Beijing, China: A case study with the WRF-Chem model,  
462 *Particuology*, 20, 32–40, doi:10.1016/j.partic.2014.06.004, 2015.
- 463 He, K., Yang, F., Ma, Y., Zhang, Q., Yao, X., Chan, C. K., Cadle, S., Chan, T. and Mulawa,  
464 P.: The characteristics of PM<sub>2.5</sub> in Beijing, China, *Atmos. Environ.*, 35(29), 4959–4970,  
465 doi:10.1016/S1352-2310(01)00301-6, 2001.
- 466 Hong, S. Y. and Lim, J.: The WRF single-moment 6-class microphysics scheme (WSM6),  
467 *Asia-Pac J. Atmos. Sci.*, 2006.
- 468 Hong, S. Y., Noh, Y. and Dudhia, J.: A new vertical diffusion package with an explicit  
469 treatment of entrainment processes, *Mon. Weather Rev.*, 134(9), 2318–2341,  
470 doi:10.1175/mwr3199.1, 2006.
- 471 Horowitz, L. W., Walters, S. and Mauzerall, D. L.: A global simulation of tropospheric ozone  
472 and related tracers: Description and evaluation of MOZART, version 2, *J. Geophys. Res.*,  
473 108(D24), 4784, doi:10.1029/2002jd002853, 2003.
- 474 Huang, R.-J., Zhang, Y., Bozzetti, C., Ho, K.-F., Cao, J.-J., Han, Y., Daellenbach, K. R.,  
475 Slowik, J. G., Platt, S. M., Canonaco, F., Zotter, P., Wolf, R., Pieber, S. M., Bruns, E. A.,  
476 Crippa, M., Ciarelli, G., Piazzalunga, A., Schwikowski, M., Abbaszade, G.,  
477 Schnelle-Kreis, J., Zimmermann, R., An, Z., Szidat, S., Baltensperger, U., Haddad, El, I.  
478 and Prévôt, A. S. H.: High secondary aerosol contribution to particulate pollution during  
479 haze events in China, *Nature*, 514(7521), 218–222, doi:10.1038/nature13774, 2014.



- 480 Kanakidou, M., Seinfeld, J. H. and Pandis, S. N.: Organic aerosol and global climate  
481 modelling: a review, *Atmos. Chem. Phys.*, 5(4), 1053–1123,  
482 doi:10.5194/acp-5-1053-2005, 2005.
- 483 Lane, T. E., Donahue, N. M. and Pandis, S. N.: Simulating secondary organic aerosol  
484 formation using the volatility basis-set approach in a chemical transport model, *Atmos.*  
485 *Environ.*, 42(32), 7439–7451, doi:10.1016/j.atmosenv.2008.06.026, 2008.
- 486 Li, G., Bei, N., Tie, X. and Molina, L. T.: Aerosol effects on the photochemistry in Mexico  
487 City during MCMA-2006/MILAGRO campaign, *Atmos. Chem. Phys.*, 11(11), 5169–  
488 5182, doi:10.5194/acp-11-5169-2011, 2011a.
- 489 Li, G., Lei, W., Bei, N. and Molina, L. T.: Contribution of garbage burning to chloride and  
490 PM<sub>2.5</sub> in Mexico City, *Atmos. Chem. Phys.*, 12(18), 8751–8761,  
491 doi:10.5194/acp-12-8751-2012, 2012.
- 492 Li, G., Lei, W., Zavala, M., Volkamer, R., Dusanter, S., Stevens, P. and Molina, L. T.:  
493 Impacts of HONO sources on the photochemistry in Mexico City during the  
494 MCMA-2006/MILAGO Campaign, *Atmos. Chem. Phys.*, 10(14), 6551–6567,  
495 doi:10.5194/acp-10-6551-2010, 2010.
- 496 Li, G., Zavala, M., Lei, W., Tsimpidi, A. P., Karydis, V. A., Pandis, S. N., Canagaratna, M. R.  
497 and Molina, L. T.: Simulations of organic aerosol concentrations in Mexico City using  
498 the WRF-CHEM model during the MCMA-2006/MILAGRO campaign, *Atmos. Chem.*  
499 *Phys.*, 11(8), 3789–3809, doi:10.5194/acp-11-3789-2011, 2011b.
- 500 Li, G., Zhang, R., Fan, J. and Tie, X.: Impacts of black carbon aerosol on photolysis and  
501 ozone, *J. Geophys. Res.*, 110(D23), D23206–10, doi:10.1029/2005JD005898, 2005.
- 502 Lipsky, E. M. and Robinson, A. L.: Effects of Dilution on Fine Particle Mass and Partitioning  
503 of Semivolatile Organics in Diesel Exhaust and Wood Smoke, *Environ. Sci. Technol.*,  
504 40(1), 155–162, doi:10.1021/es050319p, 2006.
- 505 Mlawer, E. J., Taubman, S. J., Brown, P. D., Iacono, M. J. and Clough, S. A.: Radiative  
506 transfer for inhomogeneous atmospheres: RRTM, a validated correlated-k model for the  
507 longwave, *J. Geophys. Res.*, 102(D14), 16663–16682, doi:10.1029/97JD00237, 1997.
- 508 Murphy, B. N. and Pandis, S. N.: Simulating the Formation of Semivolatile Primary and  
509 Secondary Organic Aerosol in a Regional Chemical Transport Model, *Environ. Sci.*  
510 *Technol.*, 43(13), 4722–4728, doi:10.1021/es803168a, 2009.
- 511 Odum, J. R., Hoffmann, T. and Bowman, F.: Gas/particle partitioning and secondary organic  
512 aerosol yields, *Environ. Sci. Technol.*, 30(8), 2580–2585, doi:10.1021/es950943, 1996.
- 513 Pankow, J. F.: An absorption model of gas/particle partitioning of organic compounds in the  
514 atmosphere, *Atmos. Environ.*, 28(2), 185–188, doi:10.1016/1352-2310(94)90093-0, 1994.
- 515 Robinson, A. L., Donahue, N. M., Shrivastava, M. K., Weitkamp, E. A., Sage, A. M.,  
516 Grieshop, A. P., Lane, T. E., Pierce, J. R. and Pandis, S. N.: Rethinking organic aerosols:  
517 semivolatile emissions and photochemical aging, *Science*, 315(5816), 1259–1262,  
518 doi:10.1126/science.1133061, 2007.
- 519 Schell, B., Ackermann, I. J., Hass, H., Binkowski, F. S. and Ebel, A.: Modeling the formation  
520 of secondary organic aerosol within a comprehensive air quality model system, *J.*  
521 *Geophys. Res.*, 106(D22), 28275–28293, doi:10.1029/2001jd000384, 2001.
- 522 Seinfeld, J. H. and Pandis, S. N.: *Atmospheric Chemistry and Physics - From Air Pollution to*  
523 *Climate Change*, 2nd ed., John Wiley & Sons, New Jersey, 2006.



- 524 Shen, Z., Arimoto, R., Cao, J., Zhang, R. and Li, X.: Seasonal Variations and Evidence for  
525 the Effectiveness of Pollution Controls on Water-Soluble Inorganic Species in Total  
526 Suspended Particulates and Fine Particulate Matter from Xi'an, China, *J. Air Waste*  
527 *Manage.*, 58(12), 1560–1570, doi:10.3155/1047-3289.58.12.1560, 2008.
- 528 Shen, Z., Cao, J., Arimoto, R., Han, Z., Zhang, R., Han, Y., Liu, S., Okuda, T., Nakao, S. and  
529 Tanaka, S.: Ionic composition of TSP and PM<sub>2.5</sub> during dust storms and air pollution  
530 episodes at Xi'an, China, *Atmos. Environ.*, 43(18), 2911–2918,  
531 doi:10.1016/j.atmosenv.2009.03.005, 2009.
- 532 Shrivastava, M. K., Lane, T. E., Donahue, N. M., Pandis, S. N. and Robinson, A. L.: Effects  
533 of gas particle partitioning and aging of primary emissions on urban and regional organic  
534 aerosol concentrations, *J. Geophys. Res.*, 113(D18), D18301–16,  
535 doi:10.1029/2007JD009735, 2008.
- 536 Shrivastava, M. K., Lipsky, E. M., Stanier, C. O. and Robinson, A. L.: Modeling  
537 Semivolatile Organic Aerosol Mass Emissions from Combustion Systems, *Environ. Sci.*  
538 *Technol.*, 40(8), 2671–2677, doi:10.1021/es0522231, 2006.
- 539 Stein, U. and Alpert, P.: Factor Separation in Numerical Simulations, *J. Atmos. Sci.*, 50(14),  
540 2107–2115, doi:10.1175/1520-0469(1993)050<2107:fsins>2.0.co;2, 1993.
- 541 Strader, R.: Evaluation of secondary organic aerosol formation in winter, *Atmos. Environ.*,  
542 33(29), 4849–4863, doi:10.1016/s1352-2310(99)00310-6, 1999.
- 543 Sun, Y. L., Wang, Z. F., Fu, P. Q., Yang, T., Jiang, Q., Dong, H. B., Li, J. and Jia, J. J.:  
544 Aerosol composition, sources and processes during wintertime in Beijing, China, *Atmos.*  
545 *Chem. Phys.*, 13(9), 4577–4592, doi:10.5194/acp-13-4577-2013, 2013.
- 546 Sun, Y., Wang, Z., Dong, H., Yang, T., Li, J., Pan, X., Chen, P. and Jayne, J. T.:  
547 Characterization of summer organic and inorganic aerosols in Beijing, China with an  
548 Aerosol Chemical Speciation Monitor, *Atmos. Environ.*, 51(C), 250–259,  
549 doi:10.1016/j.atmosenv.2012.01.013, 2012.
- 550 Tie, X., Madronich, S., Walters, S. and Zhang, R.: Effect of clouds on photolysis and  
551 oxidants in the troposphere, *J. Geophys. Res.*, 108(D20), doi:10.1029/2003jd003659,  
552 2003.
- 553 Tie, X., Zhang, Q., He, H., Cao, J., Han, S., Gao, Y., Li, X. and Jia, X. C.: A budget analysis  
554 of the formation of haze in Beijing, *Atmos. Environ.*, 100(C), 25–36,  
555 doi:10.1016/j.atmosenv.2014.10.038, 2015.
- 556 Tsimpidi, A. P., Karydis, V. A. and Zavala, M.: Evaluation of the volatility basis-set  
557 approach for the simulation of organic aerosol formation in the Mexico City metropolitan  
558 area, *Atmos. Chem. Phys.*, 10(2), 525–546, doi:10.5194/acp-10-525-2010, 2010.
- 559 Volkamer, R., San Martini, F., Molina, L. T., Salcedo, D., Jimenez, J. L. and Molina, M. J.:  
560 A missing sink for gas-phase glyoxal in Mexico City: Formation of secondary organic  
561 aerosol, *Geophys. Res. Lett.*, 34(19), L19807–5, doi:10.1029/2007GL030752, 2007.
- 562 Wesely, M. L.: Parameterization of surface resistances to gaseous dry deposition in  
563 regional-scale numerical models, *Atmos. Environ.* (1967), 23(6), 1293–1304,  
564 doi:10.1016/0004-6981(89)90153-4, 1989.
- 565 Yang, F., Tan, J., Zhao, Q., Du, Z., He, K., Ma, Y., Duan, F., Chen, G. and Zhao, Q.:  
566 Characteristics of PM<sub>2.5</sub> speciation in representative megacities and across China, *Atmos.*  
567 *Chem. Phys.*, 11(11), 5207–5219, doi:10.5194/acp-11-5207-2011, 2011.



- 568 Yu, X. Y.: Measurements of Carbonaceous Aerosols Using Semi-Continuous  
569 Thermal-Optical Method, InTech. 2011.
- 570 Yu, X. Y., Cary, R. A. and Laulainen, N. S.: Primary and secondary organic carbon  
571 downwind of Mexico City, Atmos. Chem. Phys., 9(18), 6793–6814,  
572 doi:10.5194/acp-9-6793-2009, 2009.
- 573 Zhang, Q., Jimenez, J. L., Canagaratna, M. R., Allan, J. D., Coe, H., Ulbrich, I., Alfarra, M.  
574 R., Takami, A., Middlebrook, A. M., Sun, Y. L., Dzepina, K., Dunlea, E., Docherty, K.,  
575 DeCarlo, P. F., Salcedo, D., Onasch, T., Jayne, J. T., Miyoshi, T., Shimojo, A.,  
576 Hatakeyama, S., Takegawa, N., Kondo, Y., Schneider, J., Drewnick, F., Borrmann, S.,  
577 Weimer, S., Demerjian, K., Williams, P., Bower, K., Bahreini, R., Cottrell, L., Griffin, R.  
578 J., Rautiainen, J., Sun, J. Y., Zhang, Y. M. and Worsnop, D. R.: Ubiquity and dominance  
579 of oxygenated species in organic aerosols in anthropogenically-influenced Northern  
580 Hemisphere midlatitudes, Geophys. Res. Lett., 34(13), L13801,  
581 doi:10.1029/2007GL029979, 2007.
- 582 Zhang, Q., Quan, J., Tie, X., Li, X., Liu, Q., Gao, Y. and Zhao, D.: Effects of meteorology  
583 and secondary particle formation on visibility during heavy haze events in Beijing, China,  
584 Sci. Total Environ., 502, 578–584, doi:10.1016/j.scitotenv.2014.09.079, 2015.
- 585 Zhang, Q., Streets, D. G. and Carmichael, G. R.: Asian emissions in 2006 for the NASA  
586 INTEX-B mission, Atmos. Chem. Phys., 9(14), 5131–5153,  
587 doi:10.5194/acp-9-5131-2009, 2009.
- 588 Zhang, R., Jing, J., Tao, J., Hsu, S. C., Wang, G., Cao, J., Lee, C. S. L., Zhu, L., Chen, Z.,  
589 Zhao, Y. and Shen, Z.: Chemical characterization and source apportionment of PM<sub>2.5</sub> in  
590 Beijing: seasonal perspective, Atmos. Chem. Phys., 13(14), 7053–7074,  
591 doi:10.5194/acp-13-7053-2013, 2013.
- 592 Zhao, J., Levitt, N. P., Zhang, R. and Chen, J.: Heterogeneous Reactions of Methylglyoxal in  
593 Acidic Media: Implications for Secondary Organic Aerosol Formation, Environ. Sci.  
594 Technol., 40(24), 7682–7687, doi:10.1021/es060610k, 2006.
- 595  
596  
597  
598



599 Table 1 Simulated mass fractions of SOA in the total OA and the SOA contribution from  
 600 various formation pathways averaged over the simulation period at urban, rural and  
 601 background sites

602

Duration	Site Type	SOA Mass Fraction in OA (%)	Mass Fraction in SOA (%)			
			PSOA <sup>a</sup>	ASOA <sup>b</sup>	BSOA <sup>c</sup>	GSOA <sup>d</sup>
April 23	Urban	32.5	77.9	5.8	5.6	10.6
	Rural	36.3	80.3	5.2	5.1	9.4
	Background	58.6	86.9	4.0	5.4	3.7
April 24	Urban	34.8	80.5	6.0	8.5	5.0
	Rural	39.9	84.4	4.0	8.5	3.1
	Background	74.4	89.4	3.2	5.8	1.6
April 25	Urban	37.3	79.5	6.2	9.9	4.4
	Rural	44.1	80.7	5.3	10.3	3.7
	Background	75.7	89.2	2.4	6.8	1.6

603 <sup>a</sup> SOA from oxidation and partitioning of POA treated as semi-volatile;

604 <sup>b</sup> SOA from oxidation of anthropogenic VOCs;

605 <sup>c</sup> SOA from oxidation of biogenic VOCs;

606 <sup>d</sup> SOA from irreversible uptake of glyoxal and methylglyoxal on aerosol surfaces.

607

608

609

610



611 Table 2 OA mass concentrations and contributions from anthropogenic emissions averaged  
 612 over the simulation period at urban, rural, and background sites

	OA Mass ( $\mu\text{g m}^{-3}$ )	OA Mass Contribution (%)	
Urban			
615	Ant. <sup>a</sup>	18.2	82.4
616	Res. <sup>b</sup>	10.4	47.2
617	Tra. <sup>c</sup>	5.5	25.0
618	Ind. <sup>d</sup>	1.3	6.1
Rural			
619	Ant. <sup>a</sup>	12.8	77.3
620	Res. <sup>b</sup>	7.9	47.8
621	Tra. <sup>c</sup>	3.4	20.3
622	Ind. <sup>d</sup>	0.4	2.6
Background			
623	Ant. <sup>a</sup>	4.7	58.6
624	Res. <sup>b</sup>	2.4	30.2
625	Tra. <sup>c</sup>	1.6	19.8
626	Ind. <sup>d</sup>	0.0	0.0

627  
 628 <sup>a</sup> Ant. stands for all anthropogenic emissions;

629 <sup>b</sup> Res. stands for residential emissions;

630 <sup>c</sup> Tra. stands for transportation emissions;

631 <sup>d</sup> Ind. stands for industrial emissions.

632

633

634

635



### Figure Captions

636

637

638 Figure 1 Map showing (a) the location of Xi'an in China, (b) WRF-CHEM model  
639 simulation domain with topography and (c) geographic distributions of 13 ambient  
640 air quality monitoring stations (black triangles) and 29 enhanced sites with filter  
641 measurements (squares). The filled red, blue, and green squares represent the urban,  
642 rural, and background sites, respectively. The area surrounded by the white line in  
643 (c) is defined as Xi'an and surrounding areas.

644

645 Figure 2 Geographic distributions of anthropogenic emissions of (a) primary organic aerosol  
646 and (b) volatile organic compounds in the simulation domain. The black lines  
647 present provincial boundaries in China.

648

649 Figure 3 Spatial patterns of calculated (contours) and observed (squares) O<sub>3</sub> concentrations  
650 at 08:00 BJT and 15:00 BJT from 23 to 25 April 2013 along with wind fields (back  
651 arrows).

652

653 Figure 4 Spatial patterns of calculated (contours) and observed (squares) PM<sub>2.5</sub>  
654 concentrations at 08:00 BJT and 15:00 BJT from 23 to 25 April 2013 along with  
655 wind fields (back arrows).

656

657 Figure 5 Temporal variations of simulated (blue line) and observed (black dots) (a) O<sub>3</sub> and  
658 (b) PM<sub>2.5</sub> concentrations averaged over 13 monitoring sites in Xi'an and  
659 surrounding areas from 23 to 25 April 2013.

660

661 Figure 6 Comparisons between the predicted and measured daily (a) PM<sub>2.5</sub> and (b)  
662 elemental carbon mass concentrations at 29 sites from 23 to 25 April 2013. The 1:1,  
663 1:2 and 2:1 lines are plotted as dotted lines.

664

665 Figure 7 Spatial distributions of calculated (contours) and observed (squares) daily PM<sub>2.5</sub>  
666 (left column) and EC (right column) concentrations from 23 to 25 April 2013.

667

668 Figure 8 Spatial patterns of simulated (contours) and retrieved (squares) aerosol optical  
669 depth at 550 nm from MODIS satellite (a) at 12:00 BJT on 24 April and (b) 11:00  
670 BJT on 25 April 2013

671

672 Figure 9 Scatter plots of the simulated (a) OA, (b) POA, and (c) SOA from the traditional  
673 (blue spots) and non-traditional (red spots) SOA modules against the observations  
674 at 29 sites from 23 to 25 April 2013.

675

676 Figure 10 Temporal variations of the simulated SOA concentrations from the traditional (blue  
677 spots) and non-traditional (red spots) SOA modules in Xi'an and surrounding areas  
678 from 23 to 25 April 2013.

679

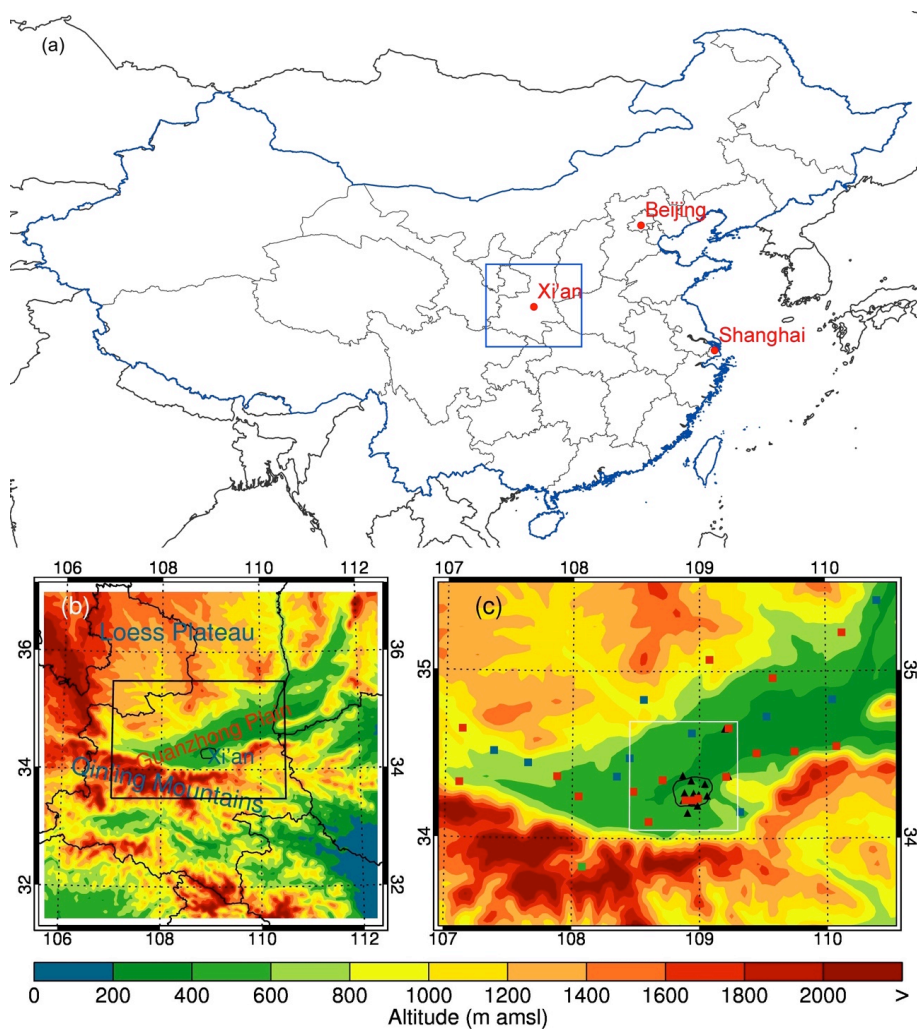
680 Figure 11 Spatial distributions of calculated (contours) and observed (squares) daily OA (left  
681 column), POA (middle column), and SOA (right column) mass concentrations from  
682 23 to 25 April 2013. Red squares in (g), (h), and (i) show the location of the  
683 background site.

684

685

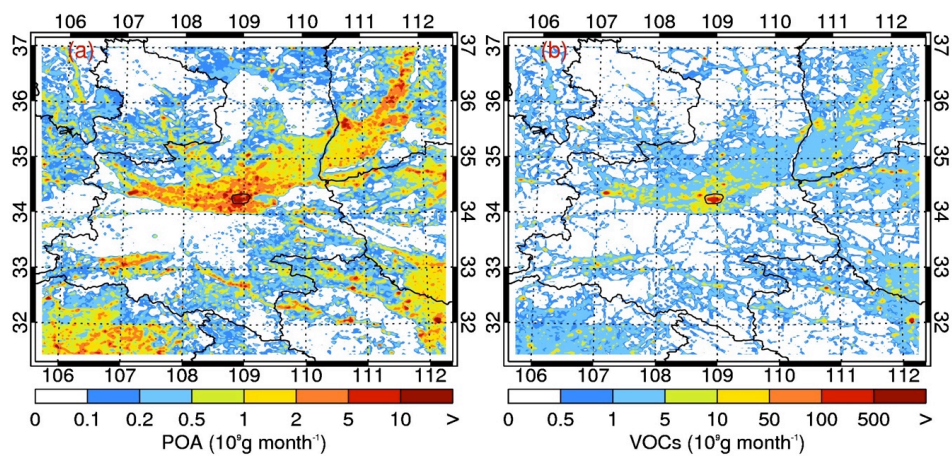


- 686 Figure 12 Comparisons between the predicted and measured daily SOA mass fraction in OA  
687 at urban, rural and background sites during the simulation episode  
688
- 689 Figure 13 The contributions of different formation pathways to SOA levels averaged over the  
690 simulation episode at (a) urban, (b) rural and (c) background sites.  
691  
692  
693  
694



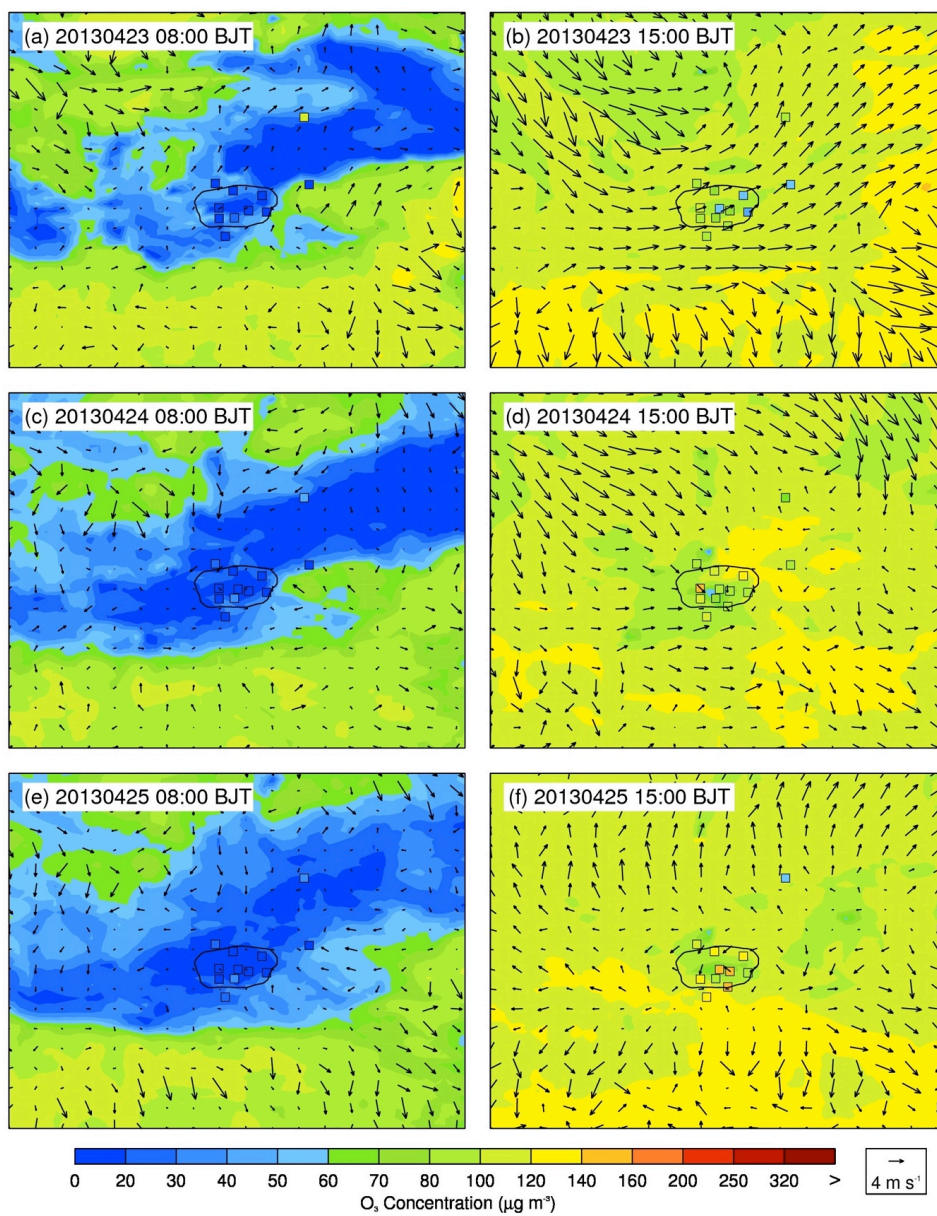
695  
696  
697  
698  
699  
700  
701

Figure 1

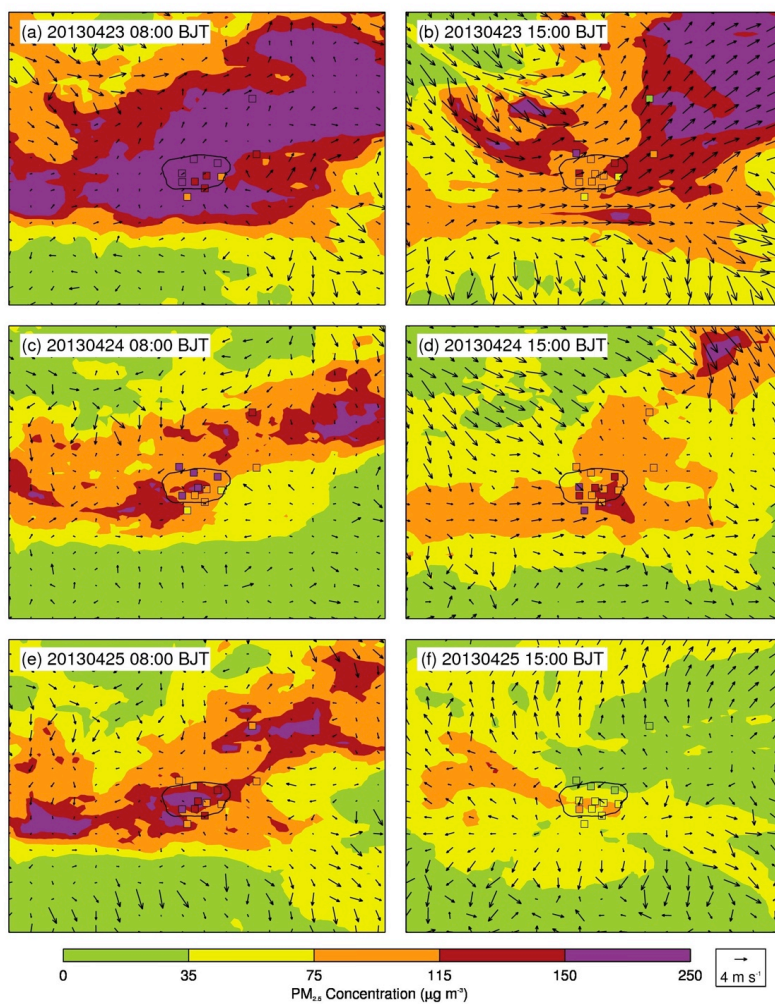


702  
703  
704  
705  
706  
707

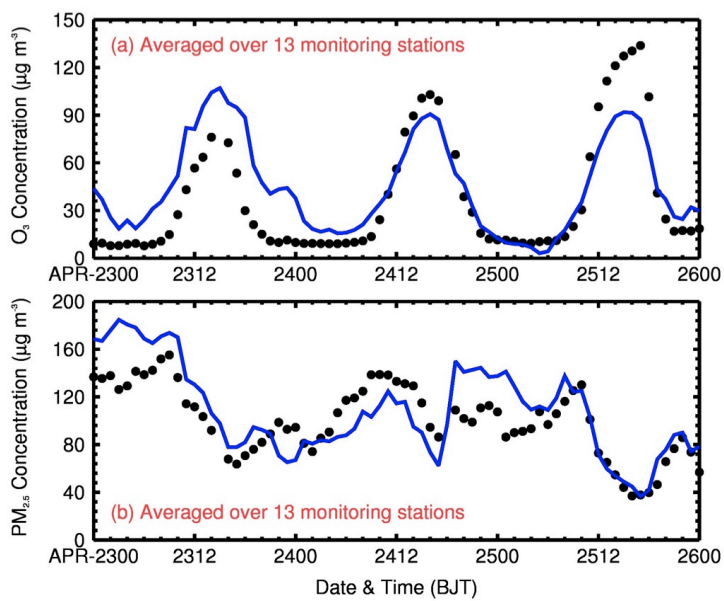
Figure 2



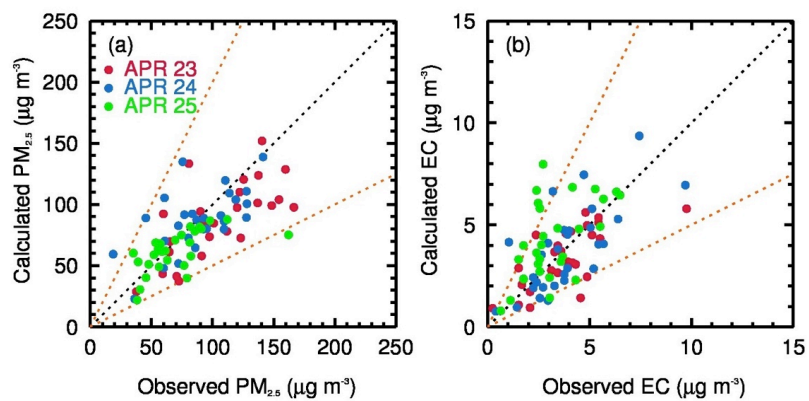
708  
709 Figure 3  
710  
711  
712  
713



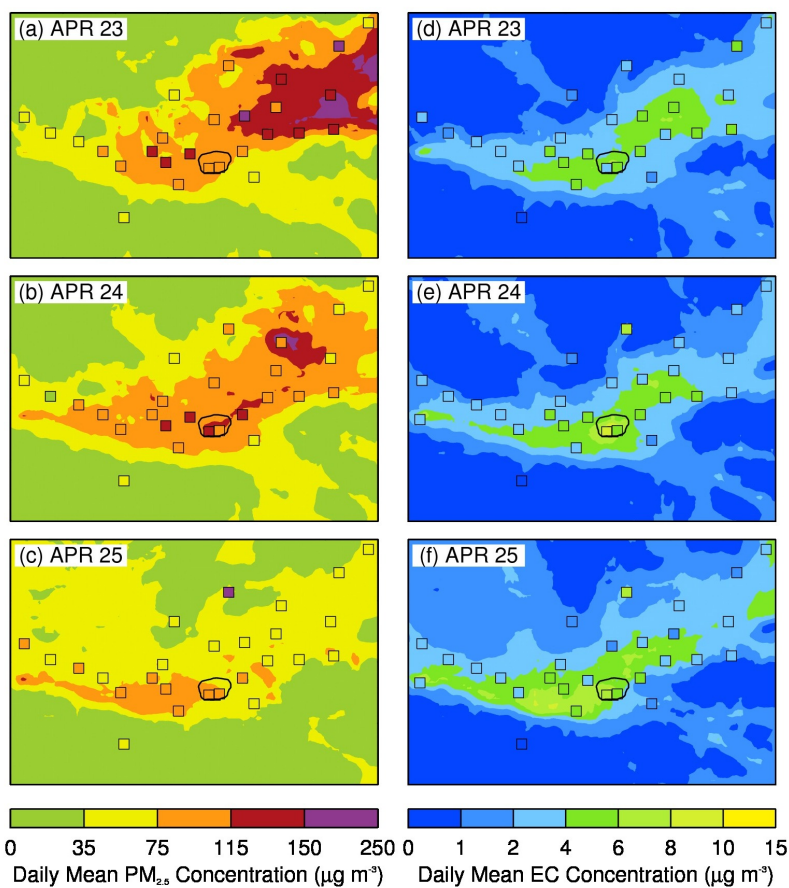
714  
715 Figure 4  
716  
717  
718  
719



720  
721 Figure 5  
722  
723  
724  
725



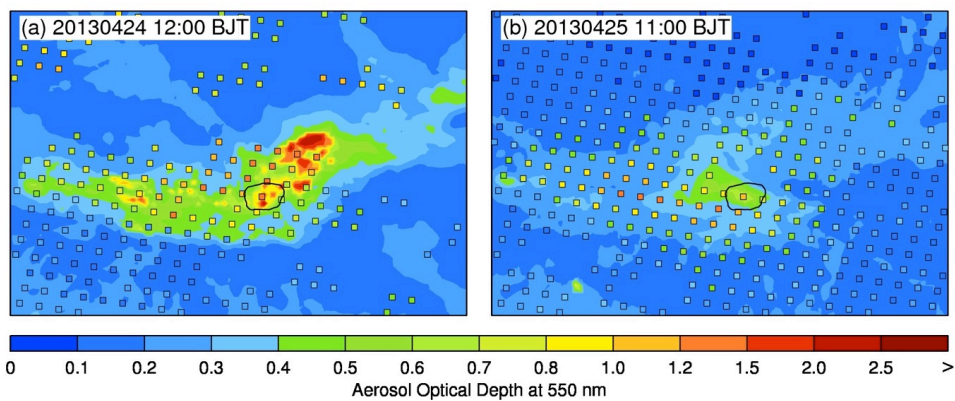
726  
727 Figure 6  
728  
729  
730  
731



732  
733 Figure 7  
734  
735  
736  
737

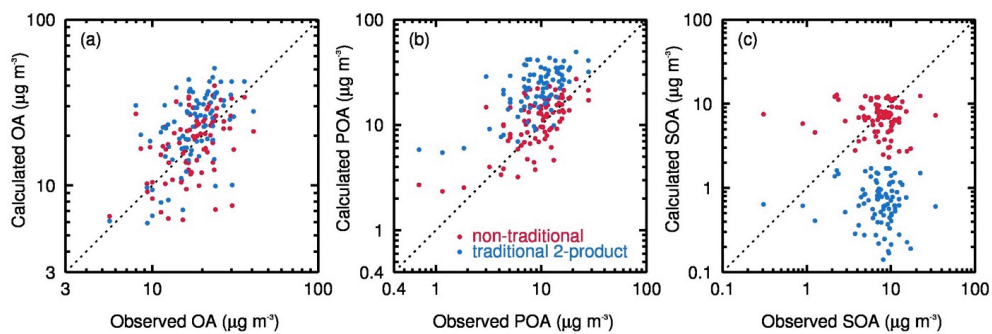


738

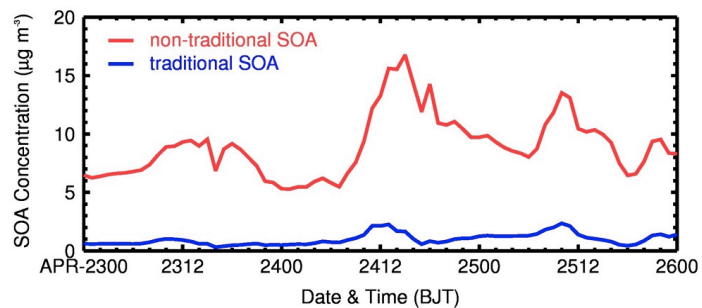


739  
740  
741  
742  
743  
744

Figure 8



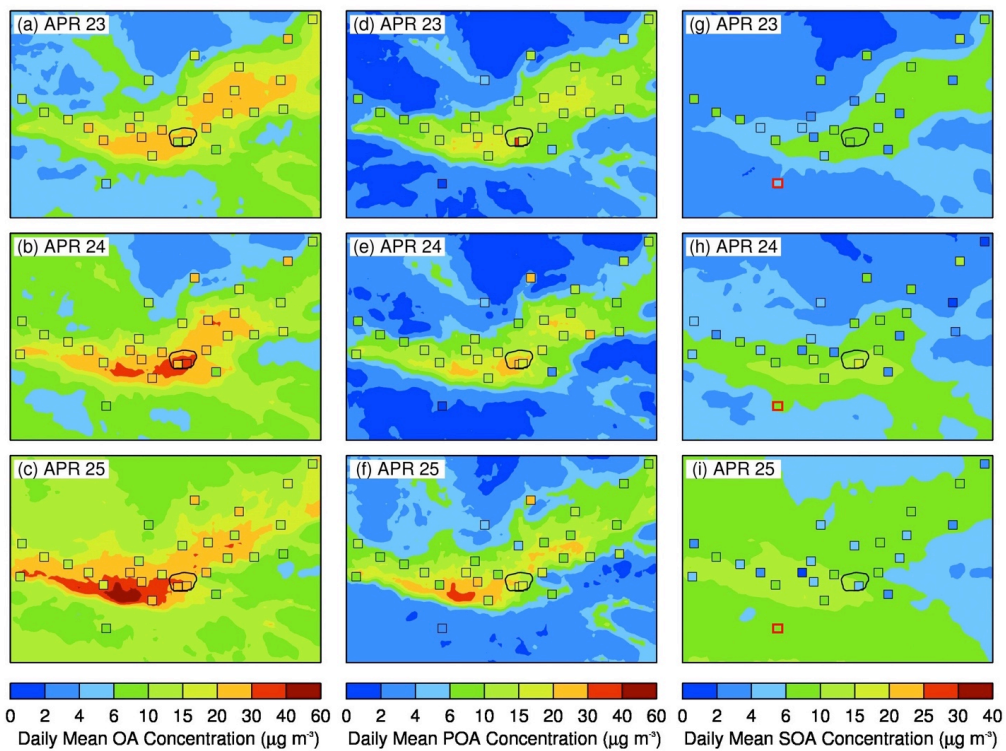
745  
746 Figure 9  
747  
748  
749  
750



751  
752 Figure 10  
753  
754  
755  
756



757

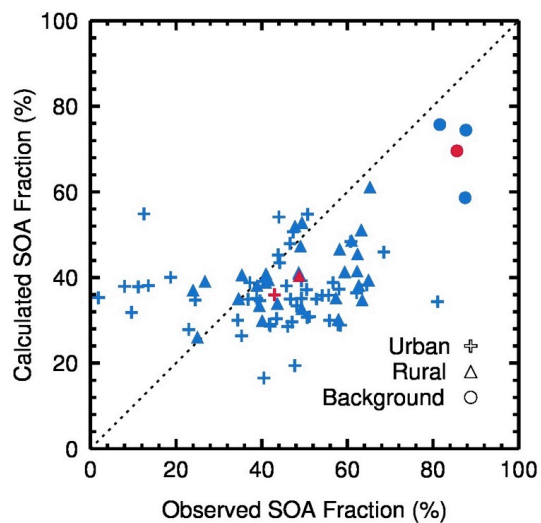


758  
759  
760  
761  
762  
763

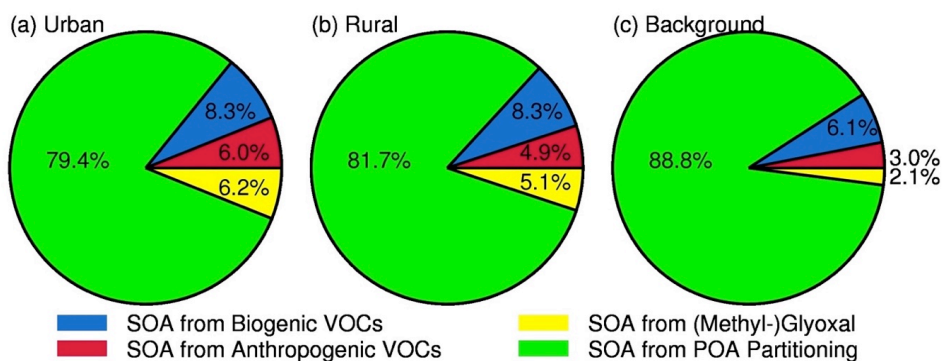
Figure 11



764



765  
766 Figure 12  
767  
768  
769  
770



771  
772 Figure 13  
773  
774  
775  
776